Physica Medica 142 (2026) 105716

Contents lists available at ScienceDirect

Physica Medica

journal homepage: www.elsevier.com/locate/ejmp

Original paper

# X-ray phase contrast imaging in GAMOS

V. Sanchez-Lara [a,*], F.R. Lozano [a,b], C. Huerga [c], Luis C. Martinez-Gomez [a,b], D. Garcia-Pinto [a]

[a] Universidad Complutense de Madrid, Madrid, 28040, Spain
[b] Hospital Universitario 12 de Octubre, Madrid, 28041, Spain
[c] Hospital Universitario La Paz, Madrid, 28046, Spain

## ARTICLE INFO

*Keywords:*
X-ray
Phase contrast
Wavefront
Monte Carlo
Simulation
Geant4

## ABSTRACT

**Objective:** X-ray Phase Contrast Imaging (PCI) enhances image contrast for weakly attenuating materials and has become increasingly relevant in biomedical and material science applications. The aim of this work is to develop and verify a Monte Carlo framework capable of realistically simulating PCI phenomena, including both refraction and wavefront propagation.

**Methods:** We have developed and integrated two complementary simulation modules within the GAMOS (GEANT4-based Architecture for Medicine-Oriented Simulations) framework. The first models refraction effects using the X-ray complex refractive index and Snell's Law. The second constructs the complex wavefront from the simulated photons and propagates it using the Fresnel formalism. Verification was carried out by simulating interferometric setups such as Young's double-slit experiment and the Talbot effect, as well as full imaging configurations for PBI and Grating-Based Imaging (GBI).

**Results:** The Snell-based simulation accurately reproduces edge-enhancement features typical of high-Fresnel-number PBI. However, in regimes where diffraction and interference dominate, the wave model yields significantly more accurate results. The agreement with theoretical predictions in all tests confirms the correct implementation of wavefront construction and propagation.

**Conclusions:** This new simulation environment extends the MIMAC platform previously developed by our group and enables realistic Monte Carlo simulations of PCI. The framework is well-suited for optimizing imaging system design, developing reconstruction algorithms, or generating synthetic datasets for Deep Learning. The combination of geometrical and wave-optical models allows flexible simulation of a wide range of PCI setups under realistic physical conditions.

Code: https://github.com/PREDICO-Project/PCI-GAMOS

## 1. Introduction

X-ray Phase Contrast Imaging (PCI) has gained significant attention over the last decade due to its ability to produce higher contrast images than conventional attenuation-based X-ray imaging, especially for samples with weak absorption (i.e., composed of low-Z elements). Unlike traditional methods that rely on X-ray absorption, PCI retrieves information about the phase shift that the object introduces to the X-ray wavefront, which is invisible in classical absorption imaging. This characteristic makes PCI particularly valuable in biomedical applications [1,2] and material science where subtle density variations need to be visualized.

Several techniques have been developed to obtain Phase Contrast images. Propagation-Based Imaging (PBI), [3,4], one of the most widely used methods, typically requires monochromatic and highly spatially coherent X-ray beams [5], with phase and absorption information being retrieved using dedicated algorithms [6–8]. Other techniques like edge illumination [9,10], speckle [11,12], or Grating-Based Imaging (GBI) [13–15] relax the coherence and energy constraints, enabling phase contrast even with polychromatic or partially coherent sources.

Despite the growing number of experimental studies and applications of PCI [16,17], its realistic simulation within Monte Carlo (MC) frameworks remains limited. Such simulations are essential for optimizing experimental setups, developing new phase retrieval algorithms, and generating robust synthetic datasets for advanced analysis, including Deep Learning applications [18,19]. Monte Carlo methods are inherently well-suited to simulate photon-matter interactions in

---

[*] Corresponding author.

*E-mail addresses:* vicsan05@ucm.es (V. Sanchez-Lara), frloza03@ucm.es (F.R. Lozano), carlos.huerga@salud.madrid.org (C. Huerga), luisc.martinez@salud.madrid.org (L.C. Martinez-Gomez), garcia.pinto@med.ucm.es (D. Garcia-Pinto).

https://doi.org/10.1016/j.ejmp.2026.105716
Received 2 August 2025; Received in revised form 24 October 2025; Accepted 1 January 2026

detail, as well as to model more complex geometries and realistic detector responses. GEANT4 [20], a general-purpose toolkit originally developed for high-energy physics, is increasingly used in low-energy applications like medical imaging.

Given that X-ray phase contrast simulation, particularly a unified framework encompassing both geometrical and wave-optical models, is not natively supported in most Monte Carlo toolkits (e.g., GEANT4, MCGPU [21,22]), and existing external implementations [23–25] typically focus on a single approximation, we have developed two independent plug-ins for GAMOS [26]. The first introduces the X-ray complex refractive index for all materials within GEANT4 and applies Snell's Law to simulate refraction effects. The second constructs the complex wavefront from the simulated photons and propagates it using the Fresnel formalism, allowing for the accurate modeling of diffraction and interference phenomena. This dual approach, uniquely integrated within a single Monte Carlo environment like GAMOS, offers unprecedented flexibility, enabling both computationally efficient simulations in the edge-enhancement regime and precise modeling of interference-dominated configurations, such as those found in GBI. This represents a significant advantage over previous works, which commonly specialize in only one of these physical approximations [24], requires external software to perform the full simulation [27] or whose implementations are not publicly available [28,29]. In contrast, the developed modules are publicly available, which not only ensures transparency and reproducibility but also adds value to the work by allowing other researchers to directly integrate, extend and check these capabilities within their own GAMOS-based studies.

This comprehensive implementation enables users to simulate realistic phase contrast imaging setups for system design, algorithm development, and synthetic data generation. The methods have been rigorously verified through direct comparison with theoretical formulations of classic wave optics experiments (Young's slits, Talbot effect), as well as full PBI and GBI simulations [30], demonstrating both qualitative and quantitative agreement with theoretical expectations.

This work builds upon our previous framework, MIMAC [31] (Mammographic Imaging Monte Carlo), originally developed as an extension of GAMOS for highly realistic conventional mammographic imaging simulations. In the present work, we use MIMAC as a foundation within the GAMOS environment to develop a new and fully compatible module that extends the capabilities of GAMOS itself to support X-ray phase-contrast imaging, incorporating new physics models and wave-optical propagation features.

## 2. Materials and methods

### *2.1. Phase contrast principles*

Considering a monoenergetic and plane X-ray beam generated by a source, the wave field is propagated from the source to the sample, interacts with the sample, and then is propagated from the sample to the detector. The propagation of the electromagnetic field is considered to happen in the absence of matter (free space propagation). The paraxial approximation is also considered. In the near-field approximation, the Fresnel propagator can be used to obtain the wave field at a certain distance.

The interaction of the X-rays with the matter can be described through the complex refractive index of the sample at each spatial point $\mathbf{r} = (x, y, z)$ [32] (see Eq. (1)).

$$n(\mathbf{r}) = 1 - \delta(\mathbf{r}) + i\beta(\mathbf{r}), \tag{1}$$

The parameters of Eq. (1), $\delta(\mathbf{r})$ and $\beta(\mathbf{r})$ are small compared to the unity. In the context of diagnostic energy, typical orders of $\delta$ are $10^{-8} - 10^{-6}$ and $\beta \approx 10^{-10} - 10^{-8}$ for low-Z materials. $\delta(\mathbf{r})$ is related to the phase effects and the imaginary part, $\beta(\mathbf{r})$, to the attenuation effects on the wave field.

The parameter $\beta$ is directly related to the linear absorption attenuation coefficient $\mu$, which quantifies the loss of intensity due to absorption and scattering. The relation is given by Eq. (2).

$$\mu(\mathbf{r}) = \frac{4\pi}{\lambda}\beta(\mathbf{r}), \tag{2}$$

where $\lambda$ is the X-ray wavelength.

The phase displacement index $\delta$ is calculated from the real part of the atomic form factor:

$$\delta = \frac{\lambda^2 r_e n_{atom}}{2\pi} f_1, \tag{3}$$

In Eq. (3), $r_e$ is the classical electron radius, $\lambda$ is the wavelength, $n_{atom}$ is the atom density, and $f_1$ is the real part of the atomic form factor [33].

Fig. 1(a) shows the values of $\delta$ and $\beta$ for water and PMMA in the energy range of radiodiagnostic, while Fig. 1(b) presents their absolute differences, $\Delta\delta$ and $\Delta\beta$. Since image contrast arises from these differences between materials, it is clear that the much larger magnitude of $\delta$ compared to $\beta$ makes phase contrast dominant over absorption contrast, particularly between low-$Z$ materials. The total phase and attenuation due to a sample can be calculated following Eq. (4).

$$\begin{aligned} \Phi(x, y) &= -\frac{2\pi}{\lambda}\int_{object} \delta(x, y, z)\, dz, \\ B(x, y) &= \frac{2\pi}{\lambda}\int_{object} \beta(x, y, z)\, dz, \end{aligned} \tag{4}$$

The integrals are the linear integrals of the indexes $\delta(x, y, z)$ and $\beta(x, y, z)$ along the path of the X-ray through the object, and $\lambda$ represents the X-ray wavelength. The complex transmission function of an object can be described by Eq. (5) [32].

$$T(x, y) = \exp(-B(x, y) + i\Phi(x, y)), \tag{5}$$

This function encapsulates both the attenuation and phase shift that the X-ray wavefront undergoes as it traverses the object. By using this formulation, the imaging process can be treated as a coherent wave interaction, allowing the application of propagation models such as the Fresnel formalism.

Ultimately, the core principle of PCI involves obtaining either the total phase shift ($\Phi(x, y)$) introduced by the sample or its spatial derivatives, which reveal structural information not detectable through absorption alone.

### *2.2. Snell's Law*

When an X-ray passes through an object, it gets refracted. Assuming an interface between two different materials with complex refractive indexes following Eq. (1), the angles of incidence and refraction can be calculated using Snell's Law (Eq. (6)).

$$\left(1 - \delta_1\right) \sin\left(\theta_1\right) = \left(1 - \delta_2\right) \sin\left(\theta_2\right), \tag{6}$$

The deviation angle, $\alpha$, is on the order of nanoradians [34], and it is related to the phase introduced by the object through Eq. (7).

$$\alpha(x, y) = \frac{\lambda}{2\pi}\left|\nabla_{xy}\Phi(x, y)\right|, \tag{7}$$

Fig. 2 shows a diagram representing the refraction process in a sphere.

In the case of a plane beam, the coordinates $\left(x_1, y_1\right)$ represent the position of a refracted photon at a distance $z$ from the object, and can be approximated as:

$$\begin{aligned} x_1 &\approx x + z\alpha_x(x, y), \\ y_1 &\approx y + z\alpha_y(x, y), \end{aligned} \tag{8}$$

In Eq. (8), $(x, y)$ denote the coordinates corresponding to the projection of a photon along a straight path, i.e., the position it would reach on the detector if no refraction is considered. The angles $\alpha_x(x, y)$ and $\alpha_y(x, y)$ describe the deviation introduced by the refraction.

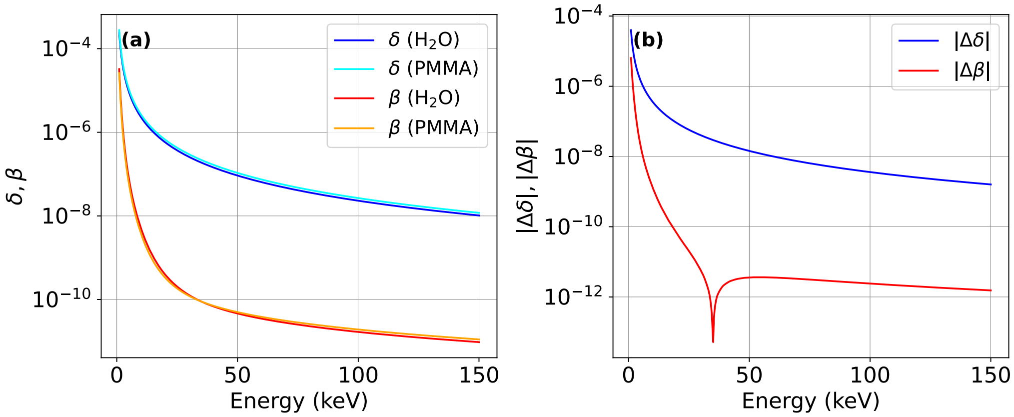

**Fig. 1.** (a) Values of $\delta$ and $\beta$ for water and PMMA in the energy range of the radiodiagnostic. (b) Absolute difference between $\delta$ and $\beta$ values between water and PMMA.

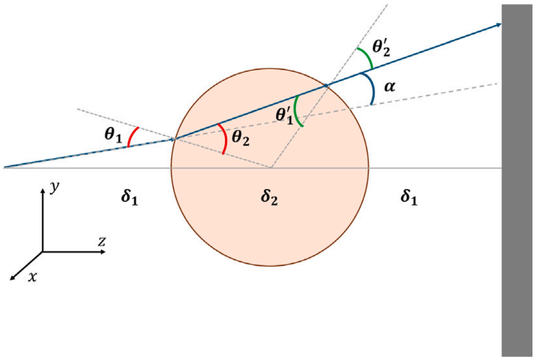

**Fig. 2.** Refraction process in a sphere.

The measured intensity at the detector position $(x_1, y_1)$, where photons arrive after being refracted, is related to the hypothetical (without refraction) intensity distribution $I(x, y)$ through the Jacobian of the coordinate transformation.

$$I\left(x_1, y_1\right) = I(x, y) \begin{vmatrix} \frac{\partial x_1}{\partial x} & \frac{\partial x_1}{\partial y} \\ \frac{\partial y_1}{\partial x} & \frac{\partial y_1}{\partial y} \end{vmatrix}^{-1}, \tag{9}$$

Under the assumption of slowly varying phase and using Eqs. (7)–(9), the intensity at the detector can be approximated by:

$$I\left(x_1, y_1\right) \approx I(x, y)\left(1 - \frac{z\lambda}{2\pi}\nabla^2 \Phi(x, y)\right), \tag{10}$$

In this expression, $I(x, y)$ is the intensity that would be observed at the detector plane in the absence of refraction. This term accounts for attenuation and can be approximated by the Beer–Lambert law.

Eq. (10) shows that the intensity at the detector plane, when refraction is considered, is proportional to the Laplacian of the phase shift introduced by the object into the wavefield. This expression can be derived from the wave nature of X-rays by solving the Helmholtz equation under the paraxial approximation for short propagation distances.

Although Snell's Law allows simulation of phase-contrast imaging (PCI) in the edge-enhancement regime, where diffraction mainly amplifies contrast at interfaces, it does not account for full wave interference [35]. To distinguish between these propagation regimes, we utilize the $F^{10}$ Fresnel number, a dimensionless parameter crucial for characterizing the diffraction behavior, as defined in Eq. (11).

$$F^{10} = \frac{(10\Delta x)^2}{\lambda z}, \tag{11}$$

where $\Delta x$ is the pixel size, $\lambda$ the X-ray wavelength and $z$ the propagation distance. If $F^{10} \gg 1$, the system is in the so-called edge-enhancement regime, where the geometrical approximation using Snell's Law remains valid. For $F^{10} \approx 1$, the system enters the Fresnel diffraction regime, and accurate simulation requires propagation of the wavefront using the Fresnel propagator [36]. Finally, when $F^{10} \ll 1$, the system approaches the Fraunhofer regime, where fine structural details are lost and diffraction dominates completely.

### 2.3. *Fresnel propagation*

Some phase-contrast imaging (PCI) techniques rely on interferometric effects, such as Talbot-Lau PCI or long-distance propagation-based imaging (PBI). These phenomena cannot be simulated using Snell's Law alone, as it does not account for the wave nature of light. To model interference effects, it is necessary to construct the complex wavefront and propagate it through space using the Fresnel formalism.

To construct the complex wavefront, a virtual plane is defined immediately after the object ($z = 0$), consisting of $N_x \times N_y$ pixels. The field is then propagated from this plane to the detector, located at a distance $D$, using the Fresnel formalism.

When a photon reaches this virtual plane at a specific pixel (x,y) with energy ($E$) and accumulated phase ($\Phi$), it contributes to the complex wavefront according to Eq. (12).

$$\psi(x, y, z = 0) = \sqrt{E}\exp(i\Phi), \tag{12}$$

With $\Phi$ obtained using Eq. (4). The contributions of the photons are summed coherently. For each photon arriving at the same virtual plane's pixel, their wavefront contribution is summed.

$$\Psi(x, y, z = 0) = \sum \psi_n(x, y, z = 0) = \sum \sqrt{E_n}\exp\left(i\Phi_n\right), \tag{13}$$

The spatial evolution of the wavefront is governed by the Helmholtz equation. Under the Fresnel approximation (valid for small propagation distances and paraxial conditions) the wavefront at a distance D is obtained by convolving the initial wavefront with the Fresnel propagator:

$$\Psi(x, y, z = D) = \mathcal{F}^{-1}\left\{exp\left[-i\pi\lambda D\left(f_x^2 + f_y^2\right)\right] \cdot \mathcal{F}\{\Psi(x, y, z = 0)\}\right\}, \tag{14}$$

With $f_x$ and $f_y$ representing the spatial frequencies, and $\lambda$ being the wavelength. Finally, the intensity at a detector positioned at a distance D from the virtual plane is given by Eq. (15).

$$I(x, y, z = D) = |\Psi(x, y, z = D)|^2, \tag{15}$$

Propagation-Based Imaging (PBI) is a phase contrast technique in which contrast arises from free-space propagation of the X-ray wavefront after is passes through a sample. As the X-rays propagate, phase modulations induced by $\delta$ are converted into intensity variations due

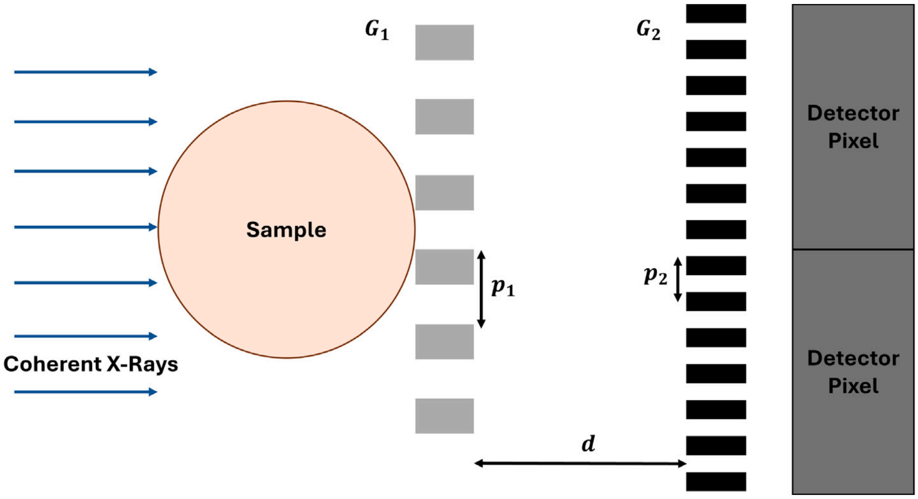

**Fig. 3.** Sketch of the Talbot-Lau interferometer used in the simulation. A coherent X-ray beam passes through the sample and a phase grating (G1), generating an interference pattern that is sampled by an absorption grating (G2) before reaching the detector. The periods $p_1$ and $p_2$, and the distance $d$, define the interferometric geometry.

to interference effects. PBI just requires a spatially coherent source and a certain distance between the sample and the detector. The degree of phase contrast observed depends on the Fresnel number (Eq. (11)). For high Fresnel numbers, the system is in the edge-enhancement regime, and the resulting image typically highlights the boundaries of structures.

### 2.4. Grating based imaging (GBI) principles

Grating-Based Imaging (GBI) is a widely used phase-contrast technique that exploits interference patterns generated by phase and absorption gratings to enhance contrast in X-ray imaging. Unlike Propagation-Based Imaging (PBI), which relies on free-space Fresnel diffraction, GBI achieves phase sensitivity through the modulation of the wavefront by periodic gratings and the analysis of the resulting Moiré patterns [37] or the phase-stepping method [38]. One of the most used setups for GBI is the Talbot-Lau interferometer, which is formed by two gratings. The first grating, G1, is a phase grating. At a certain distance from G1, an absorbing grating, G2, is placed. The detector pixels must be larger than the period of G2 (see Fig. 3).

The Talbot-Lau interferometer is based on the Talbot effect. When a coherent wavefront illuminates a periodic structure (such as a grating), self-images of the grating pattern reappear at periodic distances (Talbot distances).

The Talbot distance $D_T$ is given by:

$$D_T = \frac{2p^2}{\lambda}, \tag{16}$$

where $p$ is the grating period and $\lambda$ is the wavelength of the X-rays.

A phase grating with known phase shifts, such as $\pi$ or $\pi/2$, produces distinctive interference patterns not present in absorption gratings. These are known as fractional Talbot images and arise due to the coherent phase modulation imposed by the grating. The distances at which self-images form for phase gratings correspond to fractional Talbot distances, as described in Eq. (17).

$$z_T = \frac{m}{2\lambda}\left(\frac{p}{\eta}\right)^2, \quad m = 1, 3, 5\ldots, \tag{17}$$

where $\eta$ depends on the phase shift ($\phi$) introduced by the grating:

$$\eta = 2\frac{\phi}{\pi}, \tag{18}$$

For a $\pi$-phase grating, the resulting self-images will be shown at odd multiples of $D_t/16$, and the periodicity of this pattern is half of the original grating.

The phase-stepping method is employed to retrieve the phase shift introduced by the sample in Talbot-Lau interferometer based GBI [39]. At an odd multiple of G1's fractional Talbot distance (Eq. (17)), G2 is placed. G2 must have the same periodicity as the self-image of G1. One of the gratings is laterally displaced in small increments (phase steps) perpendicular to the grating lines.

By recording the intensity on the detector at each phase step, a modulation curve is obtained for each detector pixel [14]. In the ideal case, with perfectly coherent illumination, infinitely sharp gratings, and negligible detector blur, this modulation follows a triangular waveform.

The phase stepping method can also be understood by considering the spatial overlap between the periodic intensity pattern generated by the first grating (G1) and the absorbing grating (G2) placed at the detector plane. When the wavefront passes through G1, it forms a periodic distribution of intensity (a self-image of G1) at specific distances.

If G2 is perfectly aligned with the bright regions of this self-image, most of the X-rays are transmitted, and the detector receives a high intensity. On the other hand, if G2 is shifted such that its absorbing lines block the bright regions, the transmitted intensity drops significantly. By laterally displacing one of the gratings (typically G1 or G2) in small increments over one grating period, a periodic modulation of the detected intensity is observed. Fig. 4 illustrates the phase-stepping method.

This process results in a modulation curve that oscillates between a maximum and a minimum following Eq. (19).

$$I(x) = A + B\cos\left(\frac{2\pi x}{p} + \phi\right), \tag{19}$$

Here, $A$ is the average intensity, $B$ is the fringe visibility (modulation amplitude), $p$ is the grating period, and $\phi$ is the phase shift introduced by the sample. By fitting this sinusoidal model to the measured intensity across all phase steps, the modulation curve parameters can be obtained for each pixel. This enables the reconstruction of differential Phase Gradient (PG), Dark Field (DF), and conventional Transmission (Tr) images from the same dataset.

To extract these images, it is necessary to acquire both a reference modulation curve (without the sample) and an object modulation curve

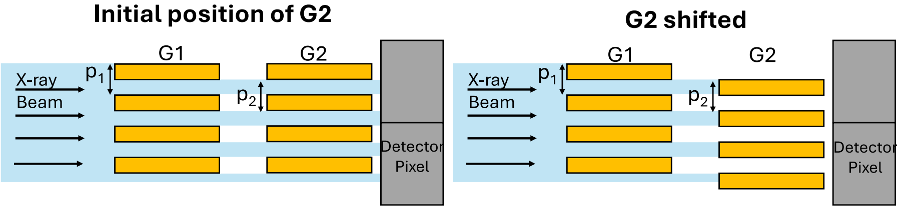

**Fig. 4.** Phase stepping principle: the absorption grating G2 is laterally shifted relative to the phase grating G1, modulating the detected intensity to extract phase contrast information.

(with the sample). The following equations are used to retrieve the three images:

$$PG = \phi_o - \phi_r,\quad Tr = \frac{A_o}{A_r},\quad DF = \frac{B_o A_r}{B_r A_o}, \tag{20}$$

## 2.5. Monte Carlo implementation

To enable realistic simulation of phase contrast imaging (PCI) within GAMOS, we developed two dedicated components: a discrete GEANT4 process (`RefractionXRay`) to model X-ray refraction at material boundaries using Snell's Law, and a GAMOS user action (`GetWavefront`) to construct and propagate the complex wavefront using the Fresnel formalism. These modules allow seamless integration of geometrical and wave-optical effects within the same Monte Carlo framework.

The first part of the work is to define the complex refractive index for all GEANT4 materials. The attenuation index $\beta$ is already implemented in all GEANT4-based toolkits through the attenuation coefficient. The phase displacement index $\delta$ is calculated from the real part of the atomic form factor through Eq. (3).

The values of $(1-\delta)$ for each energy and material used in the simulation are uploaded to the simulation through the `RINDEX` GEANT4 property from text files for each element.

The materials used in each simulation are retrieved using the `GetMaterialTable` method. For materials composed of a single element, the real part of the refractive index is directly extracted from the corresponding text file. For compound materials, the real part of the refractive index is calculated using Eq. (21), where $w_i$ is the mass fraction of element $i$.

$$\frac{\delta}{\rho} = \sum_{i=0}^{N} w_i \frac{\delta_i}{\rho_i}, \tag{21}$$

The process of retrieving the materials used in the simulation and populating the `RINDEX` property is performed during the initialization of the simulation. A folder containing the refractive indices of all elements, precomputed using Eq. (3), is used to streamline this process. This approach allows for fast implementation of the real part of the refractive index and eliminates the need to recompile the code when the materials used in the simulation change.

While Snell's Law is already available for optical photons (`G4OpBoundaryProcess`), we extended its applicability to X-rays by implementing it within a custom GEANT4 Physics List (`PCIPhysicsList`). `PCIPhysicsList` uses the `G4EmStandardPhysics_option4` physics list for electromagnetic processes and the standard transportation method (`G4Transportation`) to describe the particle motion. A new discrete process, `RefractionXRay`, is added to incorporate the real part of the refractive index and Snell's Law.

The flowchart of the `RefractionXRay` process is outlined as follows. At the end of each particle step (`PostStepDoIt`), the start (`PreStepPoint`) and end (`PostStepPoint`) points of the step are recorded. If the endpoint lies on a geometry boundary, Snell's Law is triggered (see Fig. 5). When this occurs, the real part of the refractive index is retrieved for both materials, and Eq. (6) is used to adjust the particle's direction. The process also accounts for total internal reflection, which is applied when $\sin\theta_2 \geq 1$. To save computation time, the refractive index of all materials used in the simulation is stored into a vector at the beginning of the simulation.

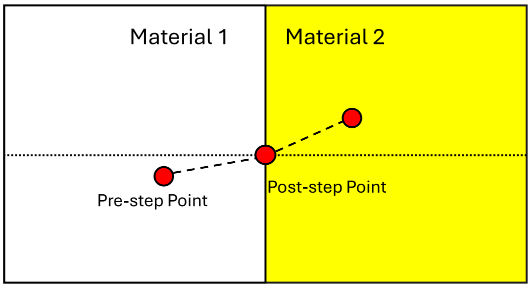

**Fig. 5.** Snell's Law in GEANT4.

`GetWavefront` module has been developed to perform the Fresnel propagation. The first step is to define a virtual plane, specifying the number of pixels and their size in the X and Y directions using the following commands:

```
/gamos/setParam GetWavefront:gridX GRIDX
/gamos/setParam GetWavefront:gridSizeX GRIDSIZEX
```

The position of the virtual plane along the Z axis is set as:

```
/gamos/setParam GetWavefront:zVirtualPlane ZPOSITION
```

By default, the virtual plane is centered at (0,0), but it can be displaced using:

```
/gamos/setParam GetWavefront:VirtualPlaneDisplacement DISPXDISPY
```

where the first value specifies the displacement in X (mm) and the second in Y (mm).

Photons reaching the virtual plane contribute to the wavefront according to Eq. (13). Once all events have been simulated (EndOfRunAction in GAMOS), Fresnel propagation is performed.

The process consists of the following steps:

1. **Forward FFT**: The Fourier transform of the wavefront is computed using the *fftw_plan_dft_2d* plan from the FFTW library.
2. **Multiplication in Fourier Space**: The transformed wavefront is multiplied by the Fresnel propagator.
3. **Inverse FFT**: The inverse Fourier transform is applied to obtain the propagated wavefront at the desired distance.

The propagation distance is configured with:

```
/gamos/setParam GetWavefront:PropDistance PROPDISTANCE
```

The detector size can be set using the following command:

```
/gamos/setParam GetWavefront:NumPixelsX XPIXELS
/gamos/setParam GetWavefront:NumPixelsY YPIXELS
```

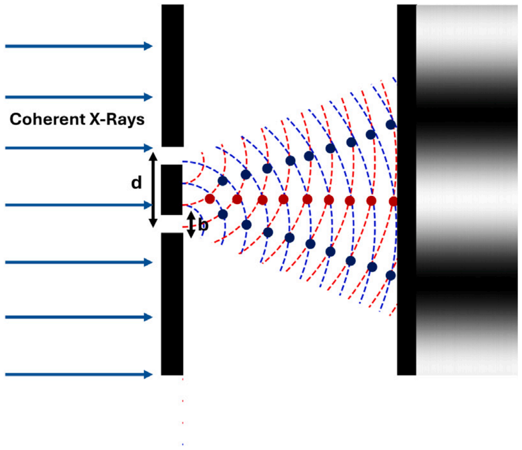

**Fig. 6.** Schematic illustration of Young's double-slit experiment. Red dots indicate regions of constructive interference, while blue dots represent regions of destructive interference.

Finally, the intensity at the detector is saved as an MHD/RAW file in a designated folder with a specified filename:

```
/gamos/setParam GetWavefront:ResultsFolder FOLDER/
/gamos/setParam GetWavefront:OutputFilename FILENAME
```

Users can select if an ideal absorbing grating is added to perform a Talbot-Lau simulation and its period, shift and angle rotation through the commands:

```
/gamos/setParam DoTalbot:Talbot 0/1
/gamos/setParam DoTalbot:PeriodG2 PERIODG2
/gamos/setParam DoTalbot:displacement DISPX DISPY DISPZ
/gamos/setParam DoTalbot:rotationAxis AXISX AXISY AXISZ
/gamos/setParam DoTalbot:rotationAngle ANGLE
```

The simulation output for both Snell's Law and Fresnel propagation consists of matrices representing the energy deposited at the detector plane (Eqs. (10) and (15)). These results are generated and further processed by a custom GAMOS module, previously developed by our team [31], which accounts for the detector material efficiency and handles the final output format.

### 2.6. Verification tests

To ensure the correct implementation of the Monte Carlo phase-contrast simulation code, a set of verification tests was performed. These tests included simulations of classical wave optics experiments with well-known analytical solutions, such as Young's double-slit and single-slit experiments, as well as the Talbot and fractional Talbot effects. The objective was to verify that the code accurately reproduces diffraction and interference patterns, validating both the wavefront generation and propagation implementation.

The schematic configuration of Young's experiment is shown in Fig. 6. The intensity distribution for the double-slit experiment as a function of the angle $\theta$ (measured from the optical axis) is given by:

$$I(\theta) = I_0 (\cos\alpha)^2 \left(\frac{sin\beta}{\beta}\right)^2, \tag{22}$$

where the parameters $\alpha$ and $\beta$ are defined as:

$$\alpha = \frac{\pi d}{\lambda}\sin\theta; \quad \beta = \frac{\pi b}{\lambda}\sin\theta, \tag{23}$$

Here, $d$ is the center-to-center distance between the two slits, $b$ is the slit width, and $\lambda$ is the wavelength of the X-rays.

We also simulated the single-slit experiment, for which the intensity is given by:

$$I(\theta) = I_0 \left(\frac{sin\beta}{\beta}\right)^2, \tag{24}$$

To further verify the correct implementation of Fresnel propagation, we simulated the self-imaging phenomenon known as the Talbot effect. For periodic objects, the wavefield reproduces the original intensity distribution at integer multiples of the Talbot distances (Eq. (16)), leading to the formation of exact self-images of the grating. In contrast, for phase-shifting gratings, the interference between diffracted orders leads to fractional Talbot images at fractional multiples of this distance (Eq. (17)), where characteristic self-images are generated. To confirm that the implemented Fresnel propagator correctly reproduces both integer and fractional Talbot effects, the so-called Talbot carpet is simulated. The Talbot carpet represents the intensity evolution along the optical axis as a function of propagation distance. Two configurations were considered: an absorption grating and a $\pi$-phase-shifting grating.

In all verification tests, the source was considered plane and monoenergetic to ensure full spatial coherence, and the detector was assumed ideal. The detailed results and quantitative comparisons with the analytical models are presented in Section 3.

### 2.7. Runtime and memory performance

All simulations were executed on an HP Z2 Tower G9 Workstation with an Intel Core i9-13900K, 32 cores and 128 GB of RAM. We repeated the same simulation while varying the number of detector pixels for the Snell-only pipeline and the grid size of the Wavefront pipeline (with fixed Field of View and pixel size rescaled accordingly).

We report two primary metrics: execution time, measured from simulation start to final image generation and peak memory usage during the simulation.

To evaluate execution time per X-ray fairly, the FFT contribution must be excluded in the Wavefront pipeline. We therefore compute $N_{\mathrm{events}}/t_{\mathrm{noFFT}}$, where $t_{\mathrm{noFFT}}$ excludes the wavefront propagation stages but includes complex grid filling.

## 3. Results

We performed several simulations to verify the implementation of `PCIPhysicsList`.

Verification of Snell's Law and Fresnel propagation modules was carried out through a series of tests involving both Propagation-Based Imaging (PBI) and Grating-Based Imaging (GBI) configurations.

### 3.1. Wavefront construction and verification

To verify our implementation of wavefront construction and Fresnel propagation in GAMOS, we simulated two classical optical experiments: Young's double-slit and single-slit experiments.

For both simulations, the X-ray source was modeled as a plane wave with an energy of 17 keV. The source was positioned 1100 mm from the object. The slits were made of lead with a thickness of 0.1 mm. In the double-slit configuration, the slit separation was 2.4 μm and each slit had a width of 0.2 μm. The detector, where the interference pattern was recorded, was positioned 200 mm from the slits.

The simulation results are presented in Fig. 7, showing a clear agreement between the theoretical predictions and the simulated intensity distributions. Quantitatively, the root-mean-square error (RMSE) between the simulated and analytical profiles is 0.8% and 2.7% for Young's double-slit and single-slit respectively.

To further verify the implementation of Fresnel wavefront propagation, we simulated the self-imaging phenomenon known as the Talbot effect.

In our simulation, a monochromatic plane wave of 20 keV illuminates a grating with a period of 10 μm and line width of 5 μm (50% duty

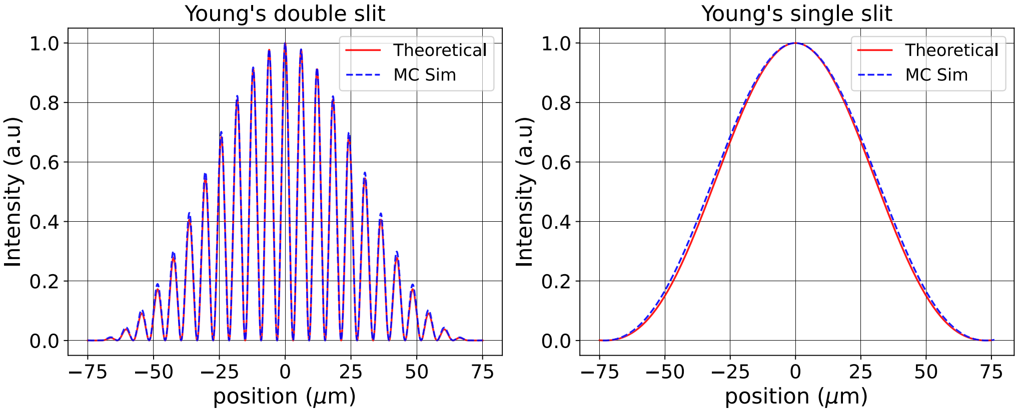

**Fig. 7.** Comparison between theoretical and simulated intensity profiles for Young's double-slit and single-slit experiments.

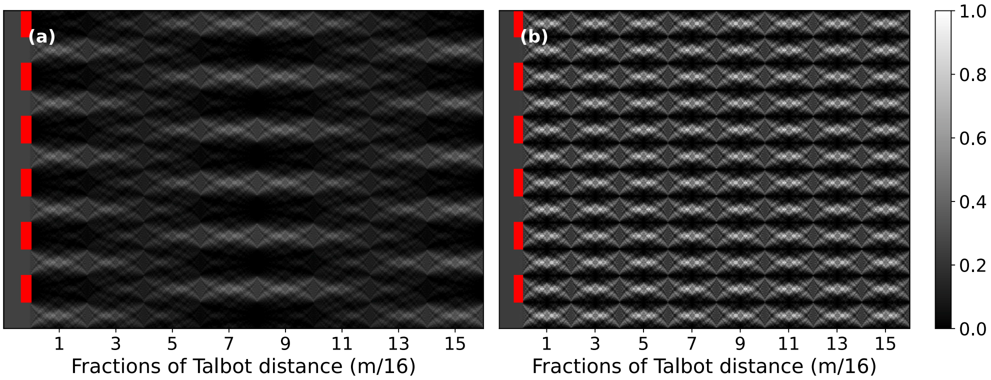

**Fig. 8.** Simulated Talbot carpet for (a) an absorption grating and (b) a $\pi$-phase shifting grating. Red bars correspond to (a) the absorbing and (b) to the phase-shifting regions. The intensity in both carpets has been normalized to the global maximum.

cycle). The detector is placed at varying distances from the grating to reconstruct the Talbot carpet. The material of the grating is lead with a thickness of 100 μm. For this configuration, the Talbot distance is 3226 mm. The results are shown in Fig. 8(a).

We also simulated the Talbot effect using a more realistic $\pi$-phase-shifting grating. The phase grating is made of Silicon with a thickness of 25.5 μm and a period of 10 μm. In this case, fractional Talbot images appear at $D_T/16$, $3D_T/16$, etc., as shown in Fig. 8(b).

These simulations reproduce the expected Talbot and fractional Talbot behavior, confirm that the wavefront propagation implemented in our Monte Carlo framework can accurately model these phenomena. Quantitative comparison with analytical Fresnel-based simulations [30] of the same configurations yields a RMSE of 0.19% for the absorption grating and 0.56% for the $\pi$-phase shifting grating, demonstrating the excellent agreement between the Monte Carlo and analytical approaches. This verification confirms that the implemented wavefront propagation can reliably reproduce self-imaging effects, enabling the simulation of Grating Based Imaging (GBI) within this framework.

### 3.2. *Propagation based Imaging (PBI)*

To evaluate the simulation of propagation-based imaging (PBI), we simulated a conical X-ray beam with an energy of 20 keV irradiating a PMMA sphere with a radius of 100 μm. The source-to-object distance was set to 40 cm, and the object-to-detector distance to 10 cm. The detector pixel size was 1 μm.

Fig. 9 presents a comparison between: (a) a wavefront-based calculation using the Fresnel propagator applied to the complex transmission function (Eqs. (5) and (14)), (b) a Monte Carlo (MC) simulation including the refraction process using the `PCIPhysicsList`, and (c) an MC simulation excluding the refraction process. All MC simulations were performed with $1 \times 10^9$ primary photons.

The MC image including refraction (Fig. 9.b) exhibits the characteristic edge enhancement typical of short distance PBI, closely matching the result obtained from the wave optics calculation (Fig. 9.a). In contrast, the MC image without refraction (Fig. 9.c), where the intensity window has been adjusted to reveal attenuation-based contrast, shows no edge enhancement.

A comparison of the intensity profiles across the three images is shown in Fig. 10, confirming the consistency between the Fresnel-based model and the Monte Carlo implementation of phase contrast.

To evaluate the correctness of the wavefront-based implementation, we performed simulations using a monochromatic plane wave source with an energy of 20 keV. The sample consists of a PMMA cylinder with a radius of 100 μm. Two configurations were considered, placing the cylinder at different distances from the detector: 10 cm and 100 cm. The pixel size in both simulations was set to 1 μm.

According to Eq. (11), the $F^{10}$ Fresnel number was 16.13 and 1.613 for the 10 cm and 100 cm propagation distances, respectively. The results are presented in Fig. 11.

Fig. 11 presents a comparative study of phase-contrast images simulated under two different propagation regimes characterized by the Fresnel number $F^{10}$. The top row corresponds to a propagation distance of 10 cm with $F^{10} = 16.13$, where edge-enhancement effects dominate and Snell's Law provides a good approximation. The bottom row shows results for a larger propagation distance of 100 cm with $F^{10} = 1.613$, approaching the Fresnel diffraction regime where interference effects become significant.

The first column (a and d) displays images obtained via analytical Fresnel propagation of the transmission function, serving as a reference.

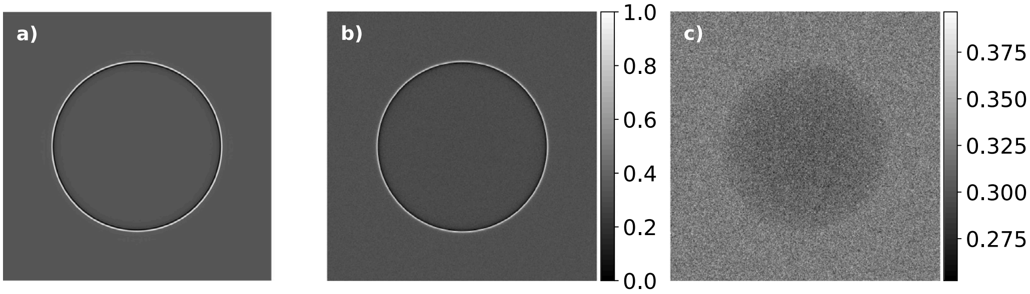

**Fig. 9.** Normalized intensity images: (a) Wavefront-based calculation using Fresnel propagation, (b) Monte Carlo simulation with refraction process, (c) Monte Carlo simulation without refraction process.

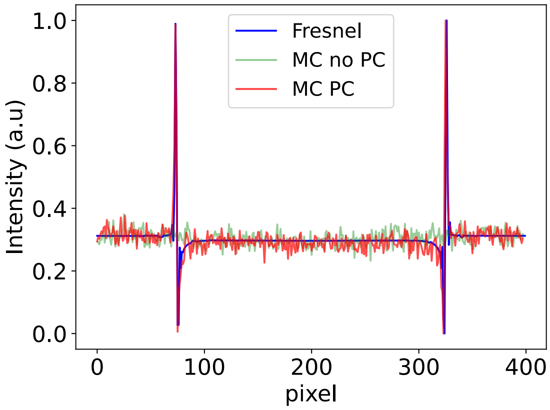

**Fig. 10.** Intensity profiles extracted from the images in Fig. 9.

The second column (b and e) shows Monte Carlo simulations incorporating Snell's Law refraction combined with Fresnel propagation of the wavefront, capturing both refraction and interference effects. The third column (c and f) presents Monte Carlo results using only Snell's Law refraction without wavefront propagation, illustrating the limitations of geometrical optics in this regime.

As expected, for the shorter propagation distance (top row), the images from MC simulations with and without propagation are very similar, highlighting the predominance of edge-enhancement contrast. For the longer distance (bottom row), notable differences appear: the MC simulation including wavefront propagation reproduces the interference pattern and contrast features observed in the analytical model, while the simulation without propagation fails to capture these effects.

The red rectangles mark the regions where intensity profiles were extracted, shown as insets within each subfigure, providing confirmation of these observations.

### 3.3. Grating based imaging (GBI)

We have implemented two different approaches to simulate Grating-Based Imaging (GBI) within our Monte Carlo framework. Both are valid under specific physical assumptions and correspond to commonly used experimental setups.

The first approach is based solely on Snell's Law refraction, without constructing or propagating the wavefront. This approximation is valid when G1 is an absorbing grating, and its periodic transmission pattern remains effectively invariant with propagation distance. The interference is encoded in the alignment between G1 and G2, and no free-space diffraction is required to form a self-image.

To test this configuration, we simulated a PMMA cylinder with an inner radius of 2 mm and an outer radius of 5 mm. The gratings G1 and G2 both have a period of 6 μm and are modeled as gold absorbing gratings. The retrieved phase gradient (PG), transmission (Tr), and dark-field (DF) images using the phase-stepping method are shown in Fig. 12.

The second approach incorporates the full wave-optical treatment by constructing the complex wavefront after interaction with a phase grating G1 and propagating it using the Fresnel formalism. In this case, the interference pattern at the detector arises from the fractional Talbot effect, and G2 must be placed at a fractional Talbot distance where a self-image of G1 is formed. This more rigorous model is essential when G1 is a phase grating, as is often the case in high-sensitivity GBI configurations.

The simulation consists of plane X-ray source with an energy of 20 keV. The sample is a hollow cylinder with an outer radius of 1 mm and an inner radius of 0.5 mm, made of water. The G1 grating is a $\pi$-phase grating made of silicon, with a thickness of 25.6 μm and a period of 2 μm. G2 is an ideal absorption grating with a period of 1 μm, positioned 8.07 mm downstream of G1 (at the first fractional Talbot distance). The retrieved images using the phase-stepping method are shown in Fig. 13.

In Fig. 14, a comparison between theoretical values and the simulated profiles of the phase gradient and transmission is shown.

The simulated images show good agreement with the theoretical predictions. The RMSE is 7.0% for the Phase Gradient image and 1.2% for the Transmission image, confirming the accurate reproduction of both attenuation and phase contrast.

### 3.4. Runtime and memory performance

Fig. 15(a) reports the execution time from the start to final image generation. Fig. 15(b) shows the peak memory usage of the simulation, both versus grid size ($N$).

As expected, the Snell-only runtime shows little dependence on the detector pixel count. In contrast, in the Wavefront case the runtime includes the allocation and filling of the complex field on the virtual plane, forward FFT, inverse FFT and final image formation. Consequently, it grows with grid size. For the configurations tested, the Wavefront pipeline is faster than Snell-only for grids below approximately $12\,000 \times 12\,000$ pixels because photons are transported only up to the virtual plane, while the FFT stages remain inexpensive at those sizes. In Snell-only, photons must be transported step by step all the way to the detector with interaction checks, upon reaching the detector, we account for detector effects using the MIMAC-based plugin [31], including efficiency (and energy to charge conversion when enabled).

Regarding memory, Snell-only usage increases with detector pixel count due to detector modeling. Wavefront requires more memory because the complex field is made by two $N \times N$ double-precision arrays (real and imaginary) and additional memory is needed during the FFT, when the peak usage occurs.

Fig. 16 shows the X-ray per second for the Wavefront and Snell-only simulations.

Higher X-rays/s are observed for the Wavefront configuration because photon transport stops at the virtual plane, whereas Snell-only transports photons to the detector and includes detector-response modeling.

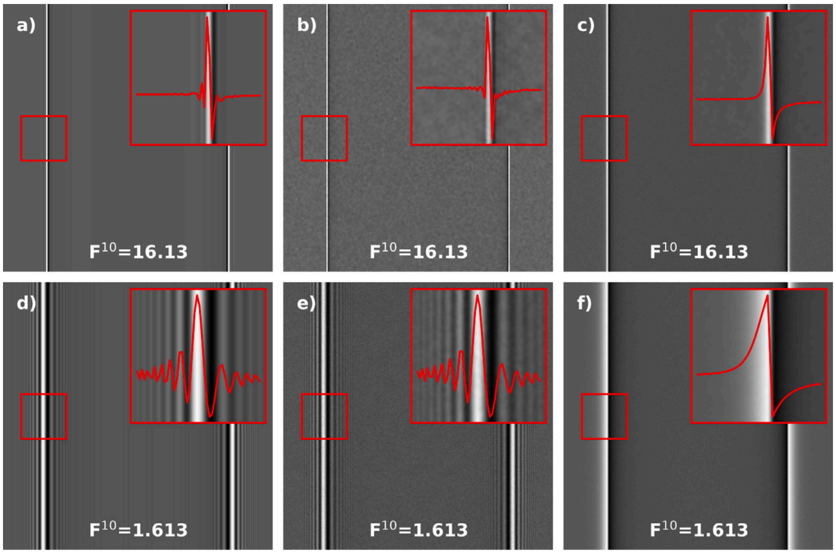

**Fig. 11.** Comparison of phase-contrast imaging (PCI) approaches for two propagation. Top row (**(a)–(c)**): Propagation distance of 10 cm ($F^{10}$ = 16.13). Bottom row (**(d)–(f)**): Propagation distance of 100 cm ($F^{10}$ = 1.613). (**(a), (d)**) Analytical Fresnel propagation of the complex transmission function. (**(b), (e)**) Monte Carlo (MC) simulation using Snell's Law with Fresnel propagation of the constructed wavefront. (**(c), (f)**) MC simulation using only Snell's Law (no propagation). Red rectangles indicate the zoomed-in region used to extract the intensity profiles shown in the insets. The images are normalized to the range 0–1.

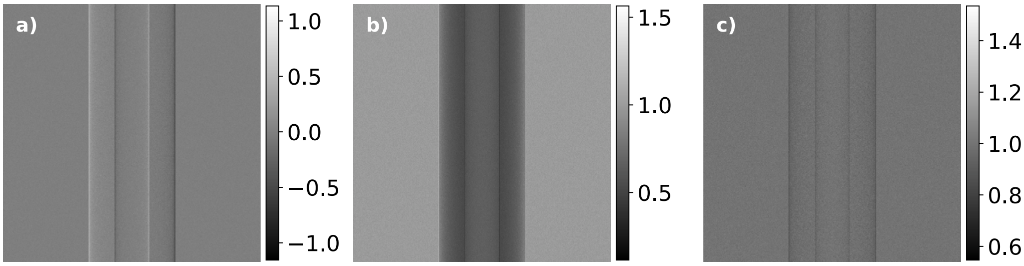

**Fig. 12.** Retrieved phase contrast images using Snell-only GBI simulation with absorbing gratings: (a) Phase Gradient, (b) Transmission, and (c) Dark Field. All images are shown in arbitrary units (a.u).

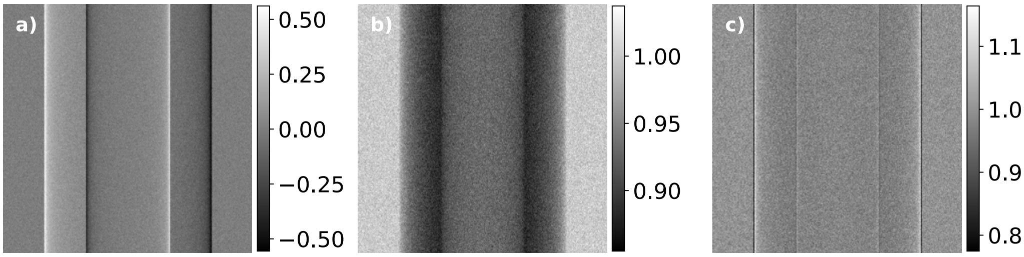

**Fig. 13.** Retrieved phase contrast images using wavefront generation and propagation GBI simulation with absorbing gratings: (a) Phase Gradient, (b) Transmission, and (c) Dark Field. All images are shown in arbitrary units (a.u).

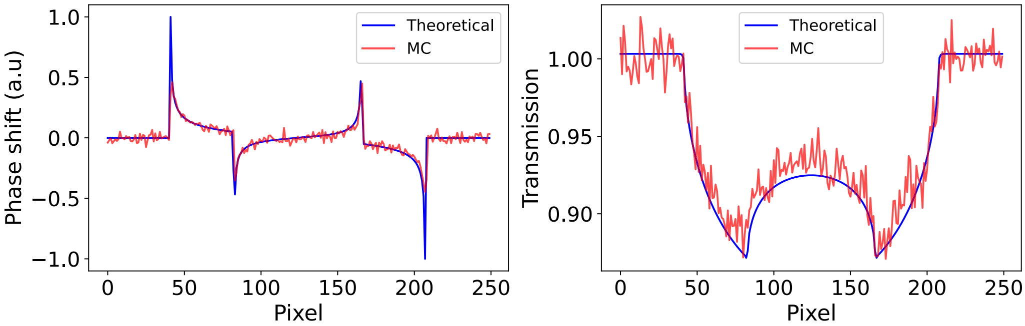

**Fig. 14.** Profiles of Fig. 13(a) and (b) compared with the theoretical values.

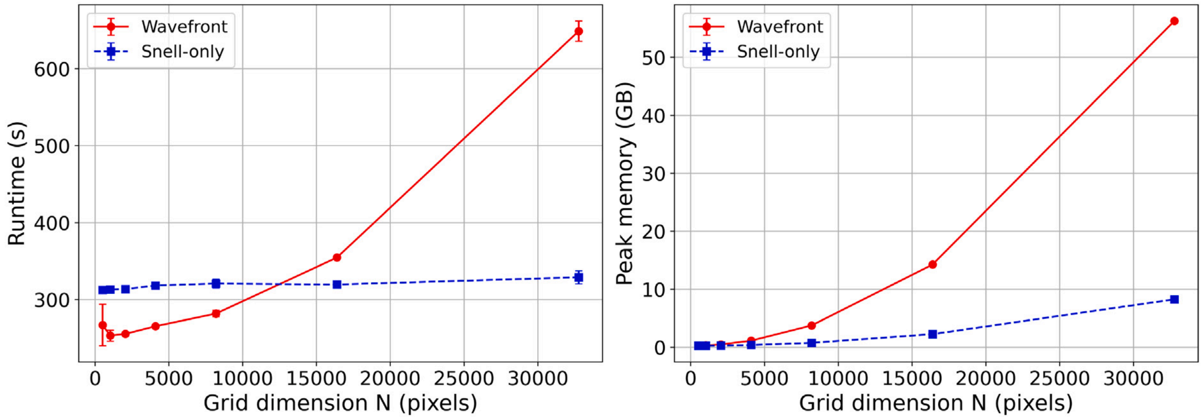

**Fig. 15.** (a) Execution time and (b) peak memory versus grid size. Error bars correspond to the standard deviation.

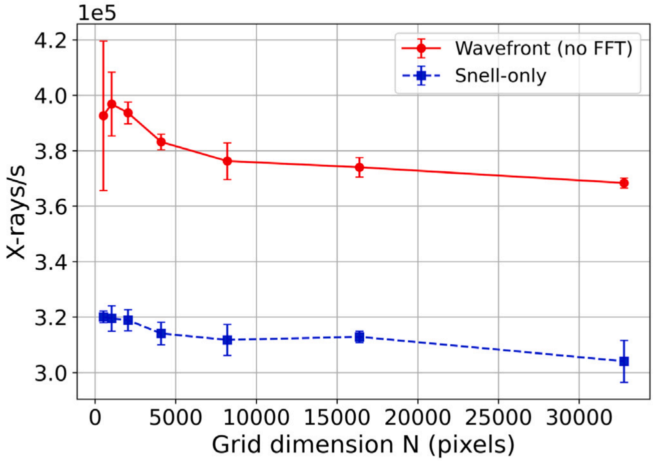

**Fig. 16.** X-rays/s versus grid size. Error bars correspond to the standard deviation.

## 4. Discussions

Our discussion begins by revisiting the fundamental verification of the implemented wave model.

Beyond the dual modeling approach and rigorous verification, our framework also significantly enhances the realism and practicality of material interactions.

Unlike some prior implementations that might rely on generic tabulated values or approximate $\delta$ as a constant, our method directly calculated the $\delta$ parameter from the real part of the atomic form factor ($f_1$) using an explicit formula (Eq. (3)). These values are then dynamically loaded from text files for all materials during initialization. This approach provides flexibility and traceability for material properties, eliminating the need for recompilation when changing material, a feature particularly valuable for diverse applications in clinical environments or material science.

The imaginary part of the refractive index, $\beta$, is directly related to X-ray attenuation. Although $\beta$ can be computed from tabulated atomic form factors of the constituent elements, these values are not directly tabulated for materials in the considered energy range and must be derived through numerical combination procedures. As a result, minor features may appear in the absolute difference of $\beta$ between materials when the dominant contribution changes from one material to another, despite the individual curves remaining continuous. In the present framework, absorption is ultimately governed by the electromagnetic interaction cross sections implemented natively in Geant4 and GAMOS, ensuring a physically consistent and robust description of attenuation.

We first thoroughly tested the correct implementation of the wavefront construction and Fresnel propagation before applying it to complex phase contrast imaging setups.

The successful reproduction of interference patterns in the simulated Young's double (and single) slit experiments with RMSE values below 3.0%, demonstrating excellent agreement with theoretical predictions (Fig. 7), rigorously confirms the accuracy of our wavefront generation method (Eq. (12)) and the successful implementation of the Fresnel propagator. Furthermore, the Talbot carpet simulations consistently reproduced the expected self-imaging effect for both absorbing and phase-shifting gratings with a RMSE values below 0.6% (Fig. 8). These comprehensive verification tests unequivocally demonstrate that the simulated wavefront evolves as expected, thereby enabling reliable simulations of Grating-Based Imaging (GBI) through the Talbot effect.

Our findings clearly demonstrate that while both the Snell's Law approximation and full wavefront propagation are capable of simulating phase contrast images, their applicability is dictated by distinct physical regimes.

For Propagation-Based Imaging (PBI), particularly at high Fresnel numbers ($F^{10} \gg 1$), Snell's Law often provides sufficient accuracy. In this regime, diffraction primarily contributes to edge sharpening, and the image contrast is predominantly governed by refraction effects. Consequently, as illustrated in Fig. 11 for $F^{10} = 16.13$, the inclusion of full wavefront propagation yields results nearly identical to those obtained with the simpler ray model. A quantitative comparison (Fig. 10) further confirms the negligible differences between the Monte Carlo simulation using only Snell's Law and the wavefront-based calculation, strongly reinforcing that for high Fresnel numbers, Snell's Law adequately reproduces the key features of the phase contrast image.

Conversely, as the Fresnel number decreases ($F^{10} \approx 1$), diffraction effects intensify, and the resulting interference patterns convey crucial image information that cannot be captured by a purely geometric model. As demonstrated in Fig. 11 (bottom row), for $F^{10} = 1.63$, the simulation based solely on Snell's Law noticeably fails to reproduce the characteristic interference fringes observed near the object's edges. In contrast, the wave-optics simulation, incorporating Fresnel propagation of the complex wavefront, accurately captures these intricate details. This unequivocally confirms the necessity of employing the full wave propagation model to correctly simulate the intensity distribution at the detector plane under low Fresnel number conditions.

For Grating-Based Imaging (GBI), the applicability of each model also depends on the grating type. The Snell's Law approximation proves effective when the first grating (G1) is an absorbing grating, as its periodic transmission pattern remains effectively invariant with propagation distance (see Fig. 4). However, when G1 is a phase grating, accurate simulation of the self-imaging phenomenon at Talbot distances, a cornerstone of GBI, is exclusively achievable through the wavefront propagation method. Our results definitively confirm that incorporating the Fresnel propagator is therefore essential to faithfully reproduce the phase-stepping modulation and to extract meaningful Phase Gradient (PG), Transmission (Tr), and Dark Field (DF) images in such configurations (see Fig. 12). As shown in Fig. 13, the phase gradient and the relative transmission are in good agreement with the theoretical values (RMSE of 7.0% and 1.2%, respectively). It should be noted, however, that the phase gradient obtained from the Monte Carlo simulation does not exactly match the amplitude of the theoretical gradient. This discrepancy arises because the theoretical gradient assumes a perfectly smooth and continuous phase profile, while the Monte Carlo model includes discretization and noise. Despite this, when the retrieved gradient is integrated to reconstruct the absolute phase, it matches the theoretical one.

While the current implementation successfully reproduces both propagation-based imaging (PBI) and Talbot-Lau grating-based imaging (GBI), several limitations remain. First, the simulations assume idealized conditions such as perfectly coherent illumination, without fully modeling the effects of partial spatial coherence often present in laboratory X-ray sources. For wave-based simulations, a monoenergetic X-ray source is assumed, which constitutes a limitation of the current model. However, this restriction only applies to the Wavefront pipeline. The Snell-only module can already operate with any source or detector model defined within GAMOS, including polyenergetic spectra and realistic detector responses such as those implemented in MIMAC [31].

The wavefront propagation module can be extended to more realistic experimental configurations. Polyenergetic spectra can be simulated by sampling the energy distribution and summing the propagated intensities, while detector imperfections (blur or noise) can be introduced through convolution with the corresponding detector point-spread function.

The Fresnel propagator implemented in this work covers a broad range of propagation conditions, from the near-field to the Fraunhofer regime. This is confirmed by the accurate reproduction of the Young's double slit interference experiment (Fig. 7). For GBI, the gratings are considered to be ideal and free of defects, and the detector is assumed to be perfect, which may not fully capture experimental imperfections. Additionally, the computational cost of full wavefront propagation is significant (Fig. 15), especially for large-scale samples with a very small grating period, potentially limiting its routine applicability. Furthermore, the current framework, MIMAC, focuses on 2D projection imaging and does not yet include capabilities for angular acquisitions or tomographic reconstructions.

## 5. Conclusions

In this work, we have successfully developed and verified two novel modules for the GAMOS toolkit, significantly expanding its capabilities for X-ray Phase Contrast Imaging. The first plug-in incorporates the complex X-ray refractive index for all GEANT4 materials and accurately models refraction through Snell's Law. The second plug-in constructs a complex wavefront from simulated photons at a virtual plane and propagates it to the detector using the Fresnel formalism. This implementation has been rigorously verified through classic wave optics experiments, including Young's double- and single-slit setups, and the simulation of the Talbot carpet for both absorbing and $\pi$-phase gratings.

This framework represents a powerful tool for various applications, including the optimization of experimental imaging system design, the development of sophisticated reconstruction algorithms and the generation of realistic synthetic datasets for Deep Learning. A key feature of our work is the flexibility it offers: users can choose between the computationally efficient Snell-based approximation, suitable for large samples and setups operating in the edge-enhancement regime, and the more demanding but essential full wave-optical simulation, indispensable for accurately reproducing interference effects characteristic of GBI or low Fresnel number conditions. Furthermore, the highly modular and fully parametrizable nature of our GAMOS plug-ins, controllable via simple commands for wavefront's grid configurations, propagation distances and outputs formats, significantly streamlines the simulation workflow. This level of automation and ease of integration into existing Monte Carlo pipelines represents a considerable advantage for researchers in medical imaging and eliminates the need for external compilation or post-processing scripts.

Both implementations expand the simulation capabilities of GAMOS and allow users to test Phase Contrast setups in a Monte Carlo environment with a level of detail not previously available in this Monte Carlo framework.

Future work will focus on optimizing memory usage to enable larger-scale simulations and on extending the wave-based simulations to polyenergetic X-ray sources and realistic detector responses. Additionally, we plan to explore the verification of simulating other prominent PCI techniques, such as speckle-based PCI, and to expand the framework to support comprehensive mammographic simulations incorporating phase contrast, thereby contributing to advanced medical imaging research.

## Funding

This work was supported by the Ministry of Science and Innovation of Spain. This work is part of the subproject of the VICTORIA project: Pre-clinical experiments for developing and optimizing new Imaging in Breast Cancer, Ref: PID2021-123390OB-C22, funded by MCIN/AEI/10.13039/501100011033.

## Declaration of competing interest

The authors declare the following financial interests that can be considered as potential competing interests: Financial support was provided by the Ministry of Science and Innovation of Spain.

## References

[1] Sarno A, Mettivier G, Golosio B, Oliva P, Spandre G, Lillo FD, Fedon C, Longo R, Russo P. Imaging performance of phase-contrast breast computed tomography with synchrotron radiation and a CdTe photon-counting detector. Phys Medica 2016;32:681–90. http://dx.doi.org/10.1016/j.ejmp.2016.04.011.

[2] Peña LA, Donato S, Bonazza D, Brombal L, Martellani F, Arfelli F, Tromba G, Longo R. Multiscale X-ray phase-contrast tomography: From breast CT to micro-CT for virtual histology. Phys Medica 2023;112:102640. http://dx.doi.org/10.1016/j.ejmp.2023.102640.

[3] Paganin D, Mayo SC, Gureyev TE, Miller PR, Wilkins SW. Simultaneous phase and amplitude extraction from a single defocused image of a homogeneous object. J Microsc 2002;206(1):33–40. http://dx.doi.org/10.1046/j.1365-2818.2002.01010.x.

[4] Gradl R, Dierolf M, Hehn L, Günther B, Yildirim AÖ, Gleich B, Achterhold K, Pfeiffer F, Morgan KS. Propagation-based phase-contrast X-ray imaging at a compact light source. Sci Rep 2017;7(1):1–9. http://dx.doi.org/10.1038/s41598-017-04739-w.

[5] Gureyev TE, Mayo SC, Myers DE, Nesterets Y, Paganin DM, Pogany A, Stevenson AW, Wilkins SW. Refracting Röntgen's rays: Propagation-based x-ray phase contrast for biomedical imaging. J Appl Phys 2009;105. http://dx.doi.org/10.1063/1.3115402.

[6] Paganin DM, Morgan KS. X-ray Fokker–Planck equation for paraxial imaging. Sci Rep 2019;9(1). http://dx.doi.org/10.1038/s41598-019-52284-5.

[7] Langer M, Zhang Y, Figueirinhas D, Forien JB, Mom K, Mouton C, Mokso R, Villanueva-Perez P. PyPhase - A python package for X-ray phase imaging. J Synchrotron Radiat 2021;28:1261–6. http://dx.doi.org/10.1107/S1600577521004951, arXiv:2012.07942.

[8] Zuo C, Li J, Sun J, Fan Y, Zhang J, Lu L, Zhang R, Wang B, Huang L, Chen Q. Transport of intensity equation: a tutorial. Opt Lasers Eng 2020;135:106187. http://dx.doi.org/10.1016/j.optlaseng.2020.106187, URL https://www.sciencedirect.com/science/article/pii/S0143816619320858.

[9] Olivo A, Speller R. Modelling of a novel x-ray phase contrast imaging technique based on coded apertures. Phys Med Biol 2007;52(22):6555. http://dx.doi.org/10.1088/0031-9155/52/22/001.

[10] Diémoz PC, Vittoria FA, Hagen CK, Endrizzi M, Coan P, Bravin A, Wagner UH, Rau C, Robinson IK, Olivo A. A single-image retrieval method for edge illumination X-ray phase-contrast imaging: Application and noise analysis. Phys Medica 2016;32:1759–64. http://dx.doi.org/10.1016/j.ejmp.2016.07.093.

[11] Zhou T, Zanette I, Zdora M-C, Lundström U, Larsson DH, Hertz HM, Pfeiffer F, Burvall A. Speckle-based x-ray phase-contrast imaging with a laboratory source and the scanning technique. Opt Lett 2015;40(12):2822–5. http://dx.doi.org/10.1364/OL.40.002822, URL https://opg.optica.org/ol/abstract.cfm?URI=ol-40-12-2822.

[12] Zdora M-C, Zanette I, Walker T, Phillips NW, Smith R, Deyhle H, Ahmed S, Thibault P. X-ray phase imaging with the unified modulated pattern analysis of near-field speckles at a laboratory source. Appl Opt 2020;59(8):2270–5. http://dx.doi.org/10.1364/AO.384531, URL https://opg.optica.org/ao/abstract.cfm?URI=ao-59-8-2270.

[13] Momose A, Kawamoto S, Koyama I, Hamaishi Y, Takai K, Suzuki Y. Demonstration of X-Ray Talbot interferometry. Japan J Appl Phys 2003;42:L866–8. http://dx.doi.org/10.1143/JJAP.42.L866.

[14] Pfeiffer F, Bech M, Bunk O, Donath T, Henrich B, Kraft P, David C. X-ray dark-field and phase-contrast imaging using a grating interferometer. J Appl Phys 2009;105(10). http://dx.doi.org/10.1063/1.3115639.

[15] Thuering T, Stampanoni M. Performance and optimization of X-ray grating interferometry. Philos Trans R Soc A 2014;372(2010). http://dx.doi.org/10.1098/rsta.2013.0027.

[16] Arboleda C, Wang Z, Jefimovs K, Koehler T, Stevendaal UV, Kuhn N, David B, Prevrhal S, Lång K, Forte S, Kubik-Huch RA, Leo C, Singer G, Marcon M, Boss A, Roessl E, Stampanoni M. Towards clinical grating-interferometry mammography. Eur Radiol 2020;30:1419–25. http://dx.doi.org/10.1007/s00330-019-06362-x.

[17] Gassert FT, Urban T, Frank M, Willer K, Noichl W, Buchberger P, Schick R, Koehler T, von Berg J, Fingerle AA, Sauter AP, Makowski MR, Pfeiffer D, Pfeiffer F. X-ray dark-field chest imaging: Qualitative and quantitative results in healthy humans. Radiology 2021;301(2):389–95. http://dx.doi.org/10.1148/radiol.2021210963.

[18] Liu P, Yang J, Chen J, Su T, Guo J, Zheng H, Liang D, Ge Y. Model-driven phase retrieval network for single-shot x-ray Talbot–Lau interferometer imaging. Opt Lett 2020;45(22):6314. http://dx.doi.org/10.1364/ol.402917.

[19] Wu Y, Zhang L, Guo S, Zhang L, Gao F, Jia M, Zhou Z. Enhanced phase retrieval via deep concatenation networks for in-line X-ray phase contrast imaging. Phys Medica 2022;95:41–9. http://dx.doi.org/10.1016/j.ejmp.2021.12.017.

[20] Agostinelli S, Allison J, Amako K, Apostolakis J, Araujo H, Arce P, Asai M, Axen D, Banerjee S, Barrand G, Behner F, Bellagamba L, Boudreau J, Broglia L, Brunengo A, Burkhardt H, Chauvie S, Chuma J, Chytracek R, Cooperman G, Cosmo G, Degtyarenko P, Dell'Acqua A, Depaola G, Dietrich D, Enami R, Feliciello A, Ferguson C, Fesefeldt H, Folger G, Foppiano F, Forti A, Garelli S, Giani S, Giannitrapani R, Gibin D, Gómez Cadenas J, González I, Gracia Abril G, Greeniaus G, Greiner W, Grichine V, Grossheim A, Guatelli S, Gumplinger P, Hamatsu R, Hashimoto K, Hasui H, Heikkinen A, Howard A, Ivanchenko V, Johnson A, Jones F, Kallenbach J, Kanaya N, Kawabata M, Kawabata Y, Kawaguti M, Kelner S, Kent P, Kimura A, Kodama T, Kokoulin R, Kossov M, Kurashige H, Lamanna E, Lampén T, Lara V, Lefebure V, Lei F, Liendl M, Lockman W, Longo F, Magni S, Maire M, Medernach E, Minamimoto K, Mora de Freitas P, Morita Y, Murakami K, Nagamatu M, Nartallo R, Nieminen P, Nishimura T, Ohtsubo K, Okamura M, O'Neale S, Oohata Y, Paech K, Perl J, Pfeiffer A, Pia M, Ranjard F, Rybin A, Sadilov S, Di Salvo E, Santin G, Sasaki T, Savvas N, Sawada Y, Scherer S, Sei S, Sirotenko V, Smith D, Starkov N, Stoecker H, Sulkimo J, Takahata M, Tanaka S, Tcherniaev E, Safai Tehrani E, Tropeano M, Truscott P, Uno H, Urban L, Urban P, Verderi M, Walkden A, Wander W, Weber H, Wellisch J, Wenaus T, Williams D, Wright D, Yamada T, Yoshida H, Zschiesche D. Geant4—a simulation toolkit. Nucl Instrum Methods Phys Res Sect A 2003;506(3):250–303. http://dx.doi.org/10.1016/S0168-9002(03)01368-8, URL https://www.sciencedirect.com/science/article/pii/S0168900203013688.

[21] Badal A, Badano A. Accelerating Monte Carlo simulations of photon transport in a voxelized geometry using a massively parallel graphics processing unit. Med Phys 2009;36:4878–80. http://dx.doi.org/10.1118/1.3231824.

[22] Badal A, Sharma D, Graff C, Zeng R, Badano A. Mammography and breast tomosynthesis simulator for virtual clinical trials. Comput Phys Comm 2020;261:107779. http://dx.doi.org/10.1016/j.cpc.2020.107779.

[23] Wang Z, Huang Z, Zhang L, Chen Z, Kang K. Implement X-ray refraction effect in Geant4 for phase contrast imaging. In: IEEE nuclear science symposium conference record. IEEE; 2009, p. 2395–8. http://dx.doi.org/10.1109/NSSMIC.2009.5402180.

[24] Brombal L, Rigon L, Arfelli F, Menk RH, Brun F. A Geant4 tool for edge-illumination X-ray phase-contrast imaging. J Instrum 2022;17(1). http://dx.doi.org/10.1088/1748-0221/17/01/C01043.

[25] Langer M, Cen Z, Rit S, Létang JM. Towards Monte Carlo simulation of X-ray phase contrast using GATE. Opt Express 2020;28(10):14522. http://dx.doi.org/10.1364/oe.391471.

[26] Arce P, Ignacio Lagares J, Harkness L, Pérez-Astudillo D, Cañadas M, Rato P, de Prado M, Abreu Y, de Lorenzo G, Kolstein M, Díaz A. Gamos: A framework to do Geant4 simulations in different physics fields with an user-friendly interface. Nucl Instrum Methods Phys Res Sect A 2014;735:304–13. http://dx.doi.org/10.1016/j.nima.2013.09.036, URL https://www.sciencedirect.com/science/article/pii/S0168900213012709.

[27] Sanctorum J, De Beenhouwer J, Sijbers J. X-ray phase contrast simulation for grating-based interferometry using GATE. Opt Express 2020;28(22):33390. http://dx.doi.org/10.1364/oe.392337.

[28] Peter S, Modregger P, Fix MK, Volken W, Frei D, Manser P, Stampanoni M. Combining Monte Carlo methods with coherent wave optics for the simulation of phase-sensitive X-ray imaging. J Synchrotron Radiat 2014;21(3):613–22. http://dx.doi.org/10.1107/S1600577514000952.

[29] Cipiccia S, Vittoria FA, Weikum M, Olivo A, Jaroszynski DA. Inclusion of coherence in Monte Carlo models for simulation of x-ray phase contrast imaging. Opt Express 2014;22(19):23480–8. http://dx.doi.org/10.1364/OE.22.023480, URL https://opg.optica.org/oe/abstract.cfm?URI=oe-22-19-23480.

[30] Sanchez-Lara V, Garcia-Pinto D. XPCIpy: A python toolkit for X-ray phase-contrast imaging. Opt Express 2025;33(22):45949–66. http://dx.doi.org/10.1364/OE.573918, URL https://opg.optica.org/oe/abstract.cfm?URI=oe-33-22-45949.

[31] Lozano F, Sanchez-Lara V, Huerga C, Martinez-Gomez LC, Garcia-Pinto D. Simulation of digital mammographic images using GAMOS: Proof of concept. Phys Medica 2025;135:104995. http://dx.doi.org/10.1016/j.ejmp.2025.104995, URL https://www.sciencedirect.com/science/article/pii/S112017972500105X.

[32] Peterzol A, Berthier J, Duvauchelle P, Ferrero C, Babot D. X-ray phase contrast image simulation. Nucl Instrum Methods Phys Res Sect B 2007;254(2):307–18. http://dx.doi.org/10.1016/j.nimb.2006.11.042.

[33] Chantler CT. Detailed tabulation of atomic form factors, photoelectric absorption and scattering cross section, and mass attenuation coefficients in the vicinity of absorption edges in the soft X-Ray (Z=30–36, Z=60–89, E=0.1 keV–10 keV), addressing convergence issues of earlier work. J Phys Chem Ref Data 2000;29(4):597–1056. http://dx.doi.org/10.1063/1.1321055, arXiv:https://pubs.aip.org/aip/jpr/article-pdf/29/4/597/11630659/597_1_online.pdf.

[34] Vila-Comamala J, Romano L, Jefimovs K, Dejea H, Bonnin A, Cook AC, Planinc I, Cikes M, Wang Z, Stampanoni M. High sensitivity X-ray phase contrast imaging by laboratory grating-based interferometry at high Talbot order geometry. Opt Express 2021;29(2):2049. http://dx.doi.org/10.1364/oe.414174.

[35] Monnin P, Bulling S, Hoszowska J, Valley J, Meuli R, Verdun F. Quantitative characterization of edge enhancement in phase contrast x-ray imaging. Med Phys 2004;31:1372–83. http://dx.doi.org/10.1118/1.1755568.

[36] Bronnikov A. Theory of quantitative phase-contrast computed tomography. J Opt Soc Amer A 2002;19:472–80. http://dx.doi.org/10.1364/JOSAA.19.000472.

[37] Bevins N, Zambelli J, Li K, Qi Z, Chen GH. Multicontrast x-ray computed tomography imaging using Talbot–Lau interferometry without phase stepping. Med Phys 2012;39(1):424–8. http://dx.doi.org/10.1118/1.3672163.

[38] Bartl P, Durst J, Haas W, Michel T, Ritter A, Weber T, Anton G. Simulation of X-ray phase-contrast imaging using grating-interferometry. In: IEEE nuclear science symposium conference record. 2009, p. 3577–80. http://dx.doi.org/10.1109/NSSMIC.2009.5401821.

[39] Kaeppler S, Rieger J, Pelzer G, Horn F, Michel T, Maier A, Anton G, Riess C. Improved reconstruction of phase-stepping data for Talbot–Lau x-ray imaging. J Med Imaging 2017;4(03):1. http://dx.doi.org/10.1117/1.jmi.4.3.034005.